Simulations of Nano-Structures in Time-Dependent External Fields

Mack Atkinson

Vanderbilt University

Advisor : Dr. Kálmán Varga

Committee:

Dr. Charles Brau

Dr. Doug Hardin

Dr. David Weintraub

1 Abstract

Time Dependent Density Functional Theory is used to probe the structure of matter. Coulomb explosion of small hydrocarbons driven by strong laser pulses and electron holography of molecules are studied in a theoretical framework. The spectra of the ejected protons obtained computationally is in good agreement with experimental data of Coulomb explosion. TDDFT allowed us to obtain time-dependent data, giving us a deeper understanding of the process. Our computational approach to electron holography provides 3-d reconstructions of simple molecules. Further investigation is needed in order to reconstruct larger molecules.

2 Introduction

2.1 Coulomb Explosion

Now that powerful laser sources are attainable, the study of their interaction with matter has become a focus of intense research interest. Various laser processes and phenomena that have become more important include, but are not limited to, high-order harmonic generation [1], creation of attosecond pulses [2], control of molecular dissociation [3], ultrafast imaging [4], electron tunneling and diffraction [5], and Coulomb explosion [6, 7]. Coulomb explosion is the process of highly energetic dissociation of a molecule due to multiple ionization. The motivation for investigating this process is that it exposes the key physical mechanisms associated with the electron and nuclear dynamics of ionization. Coulomb explosion also has practical applications such as generating bright keV x-ray photons [8, 9], generating highly energetic electrons [10], and imaging [11, 12, 13].

We study the Coulomb explosion of hydrocarbon molecules, which has also been the subject of several experimental works [7, 14, 15, 16, 17, 18]. The kinetic energy distributions of the protons ejected during fragmentation is where the most of the focus is in these experiments. Proton energies as high as 30 eV at moderate laser pulse peak intensities have been recorded for small [7] and large [14] hydrocarbon molecules. A recent experiment [7] suggests that these high proton energies originate from a high molecular charge state. These observed high charge states are thought to be caused by a multibond version of the enhanced ionization process. This process results in complete molecular fragmentation. A recent theoretical study [19] confirms the suggested ionization mechanism. While these experiments are able to find pertinent data regarding Coulomb explosion, they do not provide an extensive, dynamical description of the fragmentation process.

The present work investigates Coulomb explosion in the theoretical framework of Time Dependent Density Functional Theory (TDDFT). We investigate two different molecules, CH_4, and 1,3-butadiene, C_4H_6. It is found that the Coulomb explosion of these hydro-

carbons mainly occurs through sudden ionization followed by an all-at-once fragmentation, supporting the idea that Coulomb explosion is concerted. We are able to simulate the intramolecular electron dynamics during and after the laser pulse interacts with the molecule in the framework of real-space real-time TDDFT complemented with Ehrenfest molecular dynamics for ionic motion.

2.2 Low Energy Electron Holography

In addition to Coulomb explosion, we have also studied electron holography from a theoretical perspective. Our work is motivated by previous works [20, 21] in which holograms are obtained in low energy electron point source (LEEPS) microscopy. In LEEPS microscopy, electrons are emitted from an atomic sized point source toward a small target (could be a molecule) causing the electrons to interfere with the target. There is a screen behind the target that records the interference pattern of the electrons. This interference pattern on the screen is known as an electron hologram. It is theorized that this electron hologram can be reconstructed to make a three-dimensional image of the original target with Angstrom resolution. This imaging technique requires one angle of impact unlike other techniques such as tomography, which requires a large spectrum of angles.

We are interested in lower energy electron holography which involves electrons with energies as low as 100 eV. There is great interest in the lower energy aspect when it comes to the imaging of DNA. Current methods of imaging DNA are destructive, and some require over 10,000 images to be averaged before the structure of the DNA can be found [22]. Using this many images causes a high signal-to-noise ratio, giving a low quality image of the structure. Theoretically, low energy electron holography can non-destructively obtain the structure of these DNA using only one image.

We computationally simulate the process of obtaining the electron hologram and reconstructing the three-dimensional image borrowing from the method described in [20]. A perfectly succesful reconstruction method has not yet been found, hence motivating our

study of the processs. Simulating this computationally allows us to check the validity of this reconstruction since we control the various positions of the atoms in the molecules so that it can easily be checked whether the final 3-d image matches with the actual image of the molecule in question. We have been able to successfully reconstruct the image of a benzene molecule (C_6H_6) due to its planar nature. More complicated structures, such as bucky balls (C_{60}), are being studied but have not yet been succesfully reconstructed. The ultimate goal of these simulations is to create a method that can reconstruct any size molecule.

3 Density Functional Theory

The systems that we deal with have extremely complicated multi-electron schrodinger equations that are next to impossible to solve directly. It is through the use of Density Functional theory that we are able to succesfully deal with these monstrous equations. DFT is a very popular computational approach for solving complicated systems because of its reasonable computational cost and how well it can deal with substantial quantum systems. In order to begin discussing DFT, let us first view the Schrodinger equation for a system of N electrons.

$$[-\sum_{i=1}^{N} \frac{\hbar^2}{2m} \bigtriangledown_i^2 + \sum_{i=1}^{N} V(r_i) + \sum_{i<j}^{N} U(r_i, r_j)]\Psi = E\Psi \tag{1}$$

Note that this equation takes into account the Born-Oppenheimer Approximation, allowing the nucle to be considerd stationary. In the equation, $\Psi = \Psi(r_1, r_2, ..., r_N)$ is the many-particle wavefunction. $V(r_i) = \sum_{A=1}^{N} \frac{Z_A e^2}{|r_i - R_A|}$ is the classical potential felt by each electron due to the atomic nuclei of the system, where N is the number of atoms in the system, and Z_A and R_A are the charge and coordinate vector, respectively, of the A^{th} nucleus. $U(r_i, r_j) = \frac{e^2}{|r_j - r_i|}$ is the potential created by the electron-electron interactions. The brilliant part of DFT is replacing this complicated, many-particle wavefunction with the electron density:

$$\rho(r) = \int \Psi^*(r_1, r_2, ..., r_N)\Psi(r_1, r_2, ..., r_N) dr_2 dr_3 ... dr_N \tag{2}$$

The Hohenberg- Kohn theorems are what allow this substitution to happen. The first theorem states that the electron density uniquely determines the potential of a system, and hence all its physical properties. The second theorem states that the energy functional, $E[n] = F[n] + \int V(r)n(r)$, where $n = N\rho(r)$, and $F[n]$ is some universal functional (it does not have an explicit dependence on $V(r)$) is minimized by the true electron density of the system. These two theorems imply that the mapping from $\Psi(r_1, r_2, ..., r_N)$ to $\rho(r)$ is one-to-one, allowing us to analyze any system using the density, rather than the many-particle

wavefunction. This reduces a generally intractable problem of 3N variables to a manageable problem of ficticious, non-interacting particles under the influence of some effective external potential. In order to makes things more intuitive, we divide the energy functional into four different components,

$$E[n] = T_{KS}[n] + E_H[n] + E_{ext}[n] + E_{xc}[n] \tag{3}$$

T_{KS} is the kinetic energy operator, $E_H = \frac{n(r)n(r')}{|r-r'|}drdr'$ is the Hartree energy, representing the classical electrostatic interaction energy, $E_{ext}[n] = \int \epsilon_{ext}(r)n(r)dr$ is the external energy due to fixed ions or external electric fields, and E_{xc} is the exchange correlation energy, which accounts for the electron-electron interactions. This seperation leads to what is known as the Kohn-Sham equation.

$$(-\frac{\hbar^2}{2m} \bigtriangledown_i^2 + V_H[n(r)] + V_{ext}[n(r)] + V_{xc}[n(r)])\phi_k(r) = E_k\phi_k \tag{4}$$

Here ϕ_k is a Kohn-Sham oribital, and $n(r)$ can be constructed using combinations of the orbitals. The difficulty is that these Kohn-Sham equations have to be solved self-consistently, since there is no way to calculate n(r) directly. In order to get around this we start with an inital guess for $n(r)$ based on the system of interest. From this guess we can compute $V[n]$ which allows us to define the Hamiltonian. The Hamiltonian matrix that we find is relatively easy to diagonalize becuase the real electrons have been replaced with the fake, non-interacting electrons. The electron-electron interactions of the original electrons would make off-diagonal elements non-zero. The justification for this approximation lies in the fact that the potential of the system is uniquely determined by the electron density. We just need to make sure that $n(r)$ of the non-interacting electrons matches $n(r)$ of the original interacting electrons. After the Hamiltonian is diagonalized, it is trivial to find the eigenvectors, which correspond to the Kohn-Sham orbitals, ϕ_k. Note that at this point, the electron density is just a guess, meaning that the Hamiltonian and its eigenvectors are just rough approximations.

We can use Kohn-Sham orbitals to find a new density for the system.

$$n_{new}(r) = \sum_{i=k}^{N} |\phi_k|^2 \tag{5}$$

We can now generate a new Hamiltonian using this newfound electron density, and we solve the new Kohn-Sham equation to obtain new Kohn-Sham orbitals. This process is repeated until the elctron density converges. When convergence happens, the Kohn-Sham equations have been solved, and a good approximation of the ground-state electron density is found. This approach can also be used to find excited states of a system. Excited states are not stable, so we use Time-Dependent Density Functional Theory (TDDFT) to describe their evolution over time. TDDFT is considerably more computationally difficult than DFT, but the same motivation and theory apply. The complication arises from the fact that the electron density functional is time-dependent.

It is important to note that the crutch of these calculations is finding a good approximation for the exchange correlation energy, E_{xc}, since it cannot be known precisely except for the case of a uniform electron gas. In our computations, we use the local density approximation (LDA) which is done in the following way. First, $n(r)$ is found for a given point on our simulation grid. Then we define a uniform electron gas with the same density, having an energy $\epsilon_{xc}[n]$. This energy is assigned to that grid point, and then this process is repeated for all grid points in the simulation box. The electron density of the neighboring points is not taken into consideration. While this approximation certainly seems reckless, it assures acceptable answers. In order to obtain the total exchange correlation energy functional we simply integrate over the entire box.

$$E_{xc}[n] = \int \epsilon_{xc}(n) n(r) dr \tag{6}$$

4 Coulomb Explosion

As mentioned in the previous section, the Hamiltonian used in our simulation is:

$$H = -\frac{\hbar^2}{2m} \bigtriangledown_i^2 + V_H[n(r)] + V_{ext}[n(r)] + V_{xc}[n(r)] \tag{7}$$

In this case, the external potential is comprised of the potential due to the moving ions, V_{ions}, and the potential due to the laser electric field in the dipole approximation, $V_{laser} = r \cdot E(t)$. The laser electric field is assumed as $E(t) = E_{max} exp[-(1/2)(t - t_{peak})^2/a^2] sin(\omega t)$, polarized along x. The paramaters a and ω match those of the experiments previously mentioned, and t_{peak} = 32.5 fs. We used two values of the laser peak intensity for the CH_4 molecule: 6.7×10^{14} and 11.0×10^{14} W/cm^2 whereas due to how computationally expensive it was, we had to limit ourselves to one intensity for C_4H_6, 13.5×10^{14} W/cm^2. Each Kohn-Sham orbital was time-propogated using the evolution operator in the form of the fourth-order Taylor expansion with a small time step of 0.64 attoseconds. The total time window in our simulations was 80 fs, which is sufficient to view the dynamics and the mechanism of the proton ejection. Our simulation box size was (37.75 $\times$ 14 $\times$ 14 and 41.25 $\times$ 17.5 $\times$17.5Å for methane and 1,3-butadiene, respectively). The grid spacing was 0.25 Å. Since this was a simulation, we had a finite sized box in which everything took place. Thus, there can be a problem of ejected particles bouncing off of the walls, and interfering with the results. Since it is much too expensive to make the box extremely big so that the particles never hit the wall in the simulation time, we used a complex absorbing potential (CAP) [23] to absorb ejected particles. The CAP is of the form $V = V_0(r) + iW(r)$, where V_0 is the original (real-valued) potential of our system, and W is an arbitrary function that is chosen to be non-zero only near the boundaries of the simulation box.

Figure 1: Snapshots of the 3D electron density and ionic positions of a C_4H_6 molecule subject to a laser pulse.

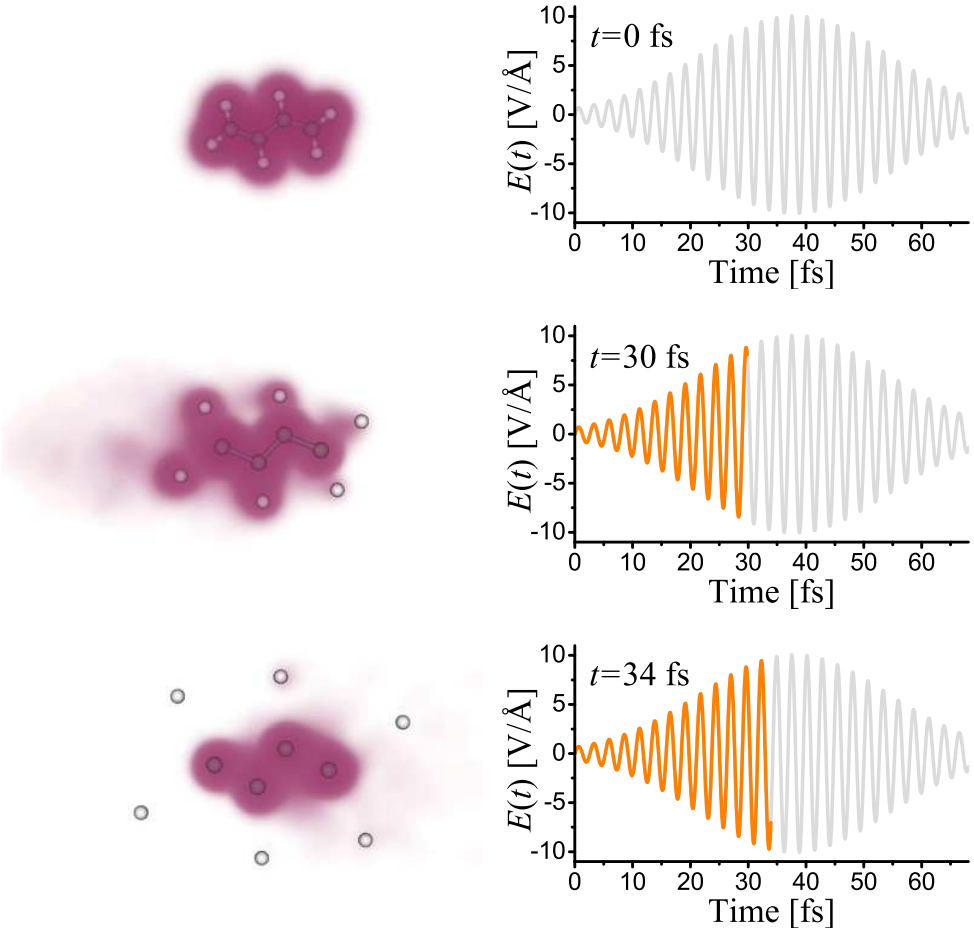

Figure 1 shows three different instances of the valence electron density and ionic positions of a C_4H_6 molecule during the interaction with the laser pulse. The first picture depicts the molecule becoming ionized, but it still keeps its structure. The second picture shows the lighter ions (protons) being simultaneously ejected radially outward from the center of the molecule. It is in the final picture that the carbon structure undergoes further ionization and explosion. For this depicted simulation, the protons are completely bare when they are ejected.

Figure 2: Number of valence electrons left in the system as a function of time for the entire ensemble of spatial configurations used in the calculations.

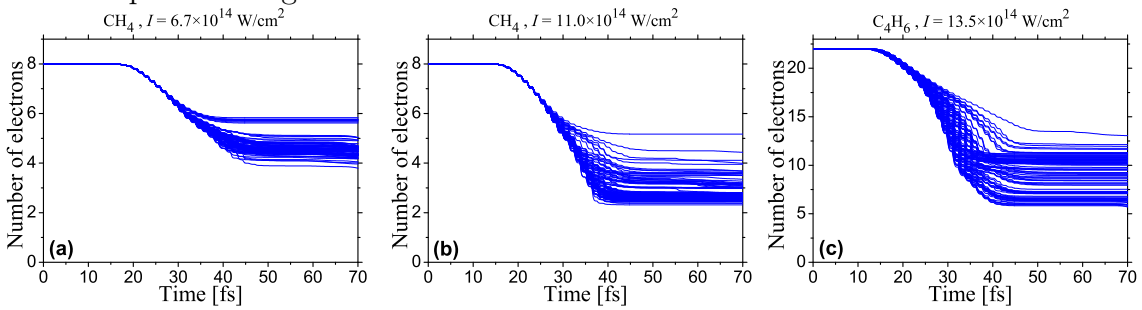

The ionization and fragmentation of a molecule in a laser electric field is strongly dependent on the spatial orientation of the molecule with respect to the field polarization axis. Figure 1 is a specific orientation of C_4H_6. Since the experiments studied the gas phase of these molecules, they are randomly oriented. This means that the measured proton spectra and charge states are distributions coming from molecules that all have different orientations. In order to account for this, we simulated 90 different orientations that covered all possible orientations, due to symmetry. This allowed us to randomize the orientations of the molecules, thus encompassing the gas phase of the molecule.

Figure 2 shows the evolution of ionization, meaning that the number of valence electrons in the two systems is plotted over time. Both molecules become strongly ionized during the pulse. The ionic charge states reach values of +5,+6 for CH_4 and +12 through +17 for C_4H_6. These ionic charge states match well with the experimentally obtained values as described in Ref. [7]. According to our simulations, molecules get more ionized when they are oriented such that there are more bonds parallel than perpendicular to the laser polarization. It is difficult to quantify a possible correlation between ionization yield and the orientation of bonds because of the different direction of the multiple bonds (both C-H and C-C).

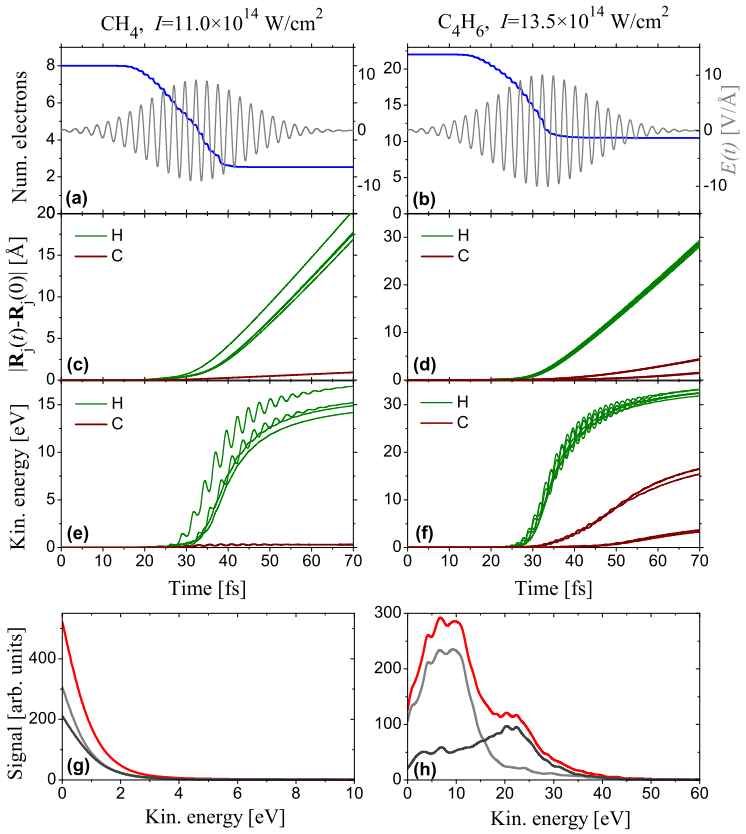

Figure 3: (a, b) Number of valence electrons remaining in the molecular system (blue lines) during ionization by a laser pulse (gray lines) for methane and 1,3-butadiene. (c, d) Displacements of individual protons (green lines) and carbon ions (dark red lines) from their initial positions. (e, f) Kinetic energies of individual protons (green lines) and carbon ions (dark red lines). While the data shown for the displacements and kinetic energies is for some randomly picked molecular spatial orientation, the same qualitative behavior could be observed for the majority of other orientations. (g, h) Measured carbon energy spectrum (red line) decomposed into the contributions of singly and doubly charged carbons (gray lines).

This strong ionization causes Coulomb explosion of the molecules. The dynamics of the ions (the displacements from the initial positions, $|R_j(t) - R_j(0)|$, and the evolution of kinetic energies are displayed in Figs. 3(c)-(f). It is evident that the molecules fragment completely in a process where all of the protons are ejected simultaneously in a concerted process. Conservation of momentum governs what directions the protons fly out from the molecules. These protons have very similar kinetic energies as can be seen in Figs. 3(e) and (f). It is important to note that these figures only show the data for one specific orientation, but the qualitative picture is the same for all orientations. Even so, any two orientations may

show final proton energies that vary substantially. For any given orientation, the final proton energies are similar along with the fact that they are ejected simultanously. The conclusion that can be obtained from this is that dynamic charge localization [24] does not apply to the fragmentaion dynamics because concerted emission of protons with similar energies is not allowed if there were a localization of charge at a specific site within the molecule.

Notice that the remaining carbon ion in the explosion of CH_4 has a near zero kinetic energy (Fig 3(e)). This is further evidence that the protons are ejected concertedly, since otherwise the carbon might have some energy. It is most prominently demonstrated that the final proton kinetic energies are similar in the simulations with the highest laser intensity performed for the C_4H_6 molecules, Figs. 3(d) and (f). After the first stage of the process when the protons are ejected simultanously, the heavy carbon structure seperates in two steps. Each step involves the explosion of two carbon ions, leading to two distinctly different final carbon energies. These two energies are clearly visible in the bimodal carbon energy spectrum in Fig. 3(h) with peaks at approximately 8 and 22 eV. We decomposed the spectrum to represent the contributions of the doubly and singly charged carbon ions, shown by the gray lines. This reveals that these two different peaks are each caused by the doubly and singly charged carbon ions, respectively. For the weaker laser peak intensity of $11.0 \times 10^{14}\mathrm{W/cm^2}$ used on the CH_4 molecule, the highly similar proton energies evident in the 1,3-butadiene simulation become less prominently displayed. Furthermore, the weakest laser peak intesity of $6.7 \times 10^{14}\mathrm{W/cm^2}$ shows a noticeable difference in the final proton energies. In fact, for certain orientations of the CH_4 molecule, a complete fragmentation was not realized in the simulation time.

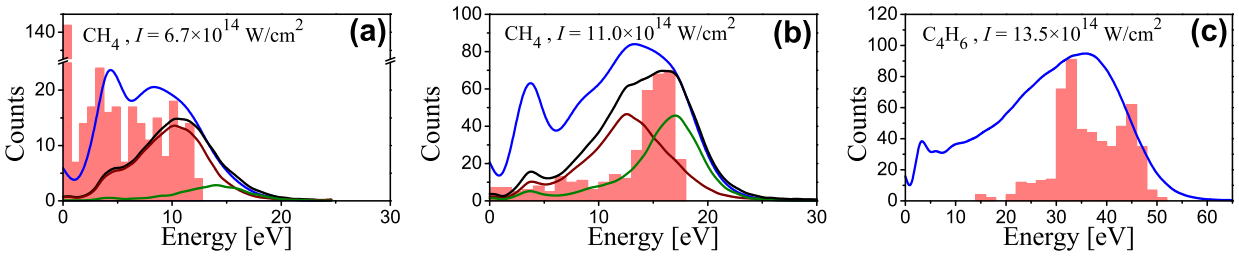

Figure 4: Histograms of computed proton energies for methane (a, b) and 1,3-butadiene (c), shown by the red bars, compared to experimentally obtained spectra (lines). The blue lines are the measured total proton energy spectra. For methane these spectra are decomposed into the contribution coming from complete molecular fragmentations (black lines) resulting in a singly (red line) and doubly (green line) charged carbon ion. Laser peak intensities are indicated in the panels.

The total proton energy spectra that model the Coulomb explosion of CH_4 and C_4H_6 are presented in Fig. 4. These histograms represent the final energies of the protons in all orientations that were simulated. There were 90 different configurations, meaning that there were 360 and 540 ejected protons for methane and 1,3-butadiene, respectively. These numbers are sufficient for creating a proper histrogram representative of the proton spectra. The uncertainty of our final proton kinetic energies is around 5% according to our calculations. This is due to the limitation of computation in that we used finite simulation time and volume. It is easy to notice that there is an early spike in the histogram for CH_4 in the lower intensity case. This is present because of the select orientations of the molecule in which protons did not detach within the 80 fs simulation time. All ejected protons have kinetic energies that are widely distributed up to the maximum value of 15 eV. There is a notable difference when viewing the histogram for the higher laser of 11.0×10^{14} W/cm^2. In this case, there is a prominent peak at around 16 eV. Also note that the cutoff energy is increased to about 18 eV. In order to understand why there is a difference between these two spectra can be understood by viewing the measured spectra. The overall spectrum in both cases exhibits a peak at around 4 eV. This is dute to protons ejected form double and triply charged methane. If only the protons created by complete fragmentation are considered, it becomes evident that the many low-energy protons in the simulation with the lower

laser peak intensity are created by incomplete molecular fragmentations. View the different colored lines in Fig 4(a) to get a nice visulization of this process. High energy protons are created only if the molecules completely fragment.

Now consider the the higher laser intesity depicted in Fig. 4(b). Almost all of the protons in this simulation are created by complete molecular fragmentations. The high-energy peak observed in the simulation agrees well with the measured protons correlated to singly and doubly charged carbon ions created during complete molecular decomposition. There is an uncertainty in determining the absolute values for the experimental pulse peak intensities. This accounts for the subtle difference in the cutoff energy.

We have shown that the protons that appear in the high energy regions of the spectrum are created by complete fragmentations only. It is clear that part of the low-energy experimental proton spectra are due to the spatial intensity distribution across the focused laser beam. The problem is that molecules that are ionized in the outer regions of this distribution are effectively exposed to a lower intensity than what is considered in the simulation. This explains part of the deviation between the measured overall proton spectrum and the decomposed spectra. This intensity smearing is not present in the simulated spectra. This causes the broad proton energy distribution in the simulated spectrum which means that high charge states are not reached for every orientation. Thus, the ionization mechanism is strongly dependent on molecular orientation relative to laser polarization.

We now discuss the case of the highest intensity laser used on C_4H_6, Fig. 4(c). There are no low energy protons evident in this spectrum. A bimodal distribution is visible, centered around 40 eV. These two observations imply that there is about a 100% chance for complete molecular fragmentation of 1,3-butadiene at this laser intensity. When comparing the simulated spectrum with the measured spectrum, we can attribute the lower energy protons to incomplete fragmentations that occur where there is a smaller intensity in the laser. Fig. 2 shows that the number of electrons detaching from the molecule have two peaks around 15-17 and 11-12. These two peaks correspond to the two peaks present in

Fig 4(c), implying that the bimodal shape comes from two strong fragmentation channels from different ionic charge states.

5 Low Energy Electron Holography

The first molecule we used to perform electron holography was benzene (C_6H_6). Before we start using TDDFT to analyze this process, we first decided to write a simpler code that assumes a simpler interaction between the electrons and the molecule. This allows us to find a reconstruction process that works without having to expend alot of computational power to run TDDFT. Once a sufficient reconstruction method is obtained, we plan on using TDDFT to find more accurate electron holograms. Our simulation box had dimensions $36 \times 32 \times 32$Å with a grid spacing of 0.2Å. It was very important to keep small grid spacing since large grid spacing meant low accuracy. This caused our simulations to be lengthy because of the high amount of grid points. The simulation spanned over 4fs, which we found to be a sufficient amount of time to obtain the electron hologram. We used a time step of 0.0001 fs so that the various interactions could be updated frequenctly. We found that higher time steps would cause divergence.

In our simulations, we represent the electron as a 1-D plane wave of the form e^{-ikx} with the low energy of 100 eV. The electron would propogate from the far left of the simulation box in the +x direction and hit the target, which was placed in the center of box. During every time step, the electron density was calculated at every grid point. In order to obtain the electron hologram, we extracted a 2-D slice of the electron density perpendicular to the motion of the electron. This 2-D slice was located 4Å to the right of the target. This 2-D slice represents the screen that records the electron hologram. Experimental works typically use a charge-coupled device with a specific spatial resolution to obtain the hologram. Fig 5 is an example of a hologram obtained from this simulation.

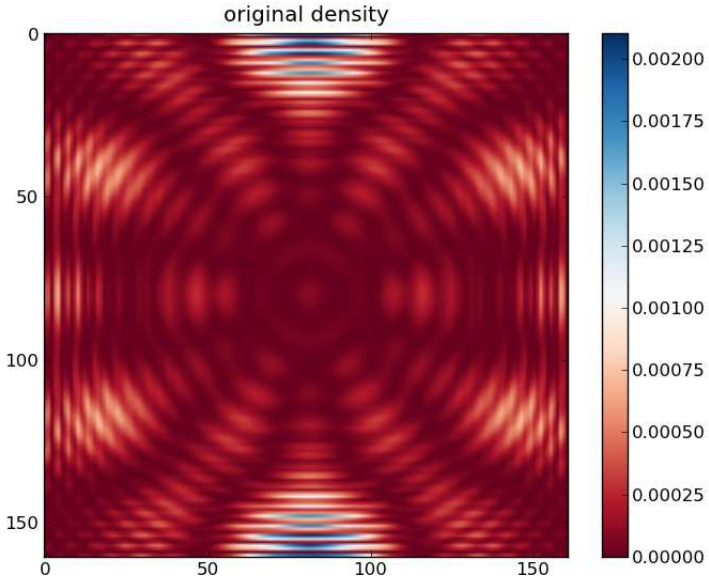

Figure 5: Electron hologram of a benzene molecule (C_6H_6) taken at the end of a 4 fs simulation.

The equation for the interference pattern is as follows:

$$I(y,z) = |e^{-ikx} + E(y,z)|^2 \tag{8}$$

where e^{-ikx} represents the electron and $E(y,z)$ is the reference wave of the molecule with which the electron interacts.

To make sure that this technique of obtaining electron holograms is working correctly, we created another simulation that generates an interference pattern from a theoretical perspective, rather than by simulating the shooting of an electron. Based on the theory presented in previous papers [20, 21], we generated a wave function on a screen, denoted as $\phi_s(\vec{\xi})$. This wave function is a result of the electron waves being scattered off the target object and interfering with the electrons that do not scatter, and it has the following form:

$$\phi_s(\vec{\xi}) = \sum_i \sum_{l,m} exp(-ik\vec{r}_i \cdot \vec{\xi}) \tau_1 Y_1^m(\hat{\xi}) F_l^m(\vec{r}_i) \tag{9}$$

where $\tau_1 = k^{-1}sin(\delta_l)exp(i\delta_l)$, $\vec{r_i}$ is the position of the ith atom, $F_l^m \approx 4_l^m(\hat{r}_i)r_i^{-1}e^{ikr_i}$, $k = 2\pi/\lambda$ is the wave number of the electron, and Y_l^m is the real form of spherical harmonics. Note that because we use a plane wave instead of a spherical wave to represent the electron, we can set l and m equal to zero, which simplifies the above equation to the following:

$$\phi_s(\vec{\xi}) = \sum_i exp(-ik\vec{r_i}\cdot\vec{\xi})\tau_0 Y_0^0(\hat{\xi})F_0^0(\vec{r_i}) \tag{10}$$

Using the fact that $Y_0^0 = 1/\sqrt{4\pi}$ we can further simplify to the following:

$$\sum_i exp(-ik\vec{r_i}\cdot\vec{\xi})\tau_0 r_i^{-1}e^{ikr_i} \tag{11}$$

where we set $\delta = 0.1$. In order to obtain the interference pattern from this wave function, the following equation is necessary:

$$I(\vec{\xi}) = \frac{1}{r^2}(e^{-ikx} + \psi_s)^2 - |e^{-ikx}|^2 \tag{12}$$

This equation can be simplified to the following form:

$$I(\vec{\xi}) = \frac{L}{r^3}(2Re(\phi_s(\vec{\xi}) + |\phi_s(\vec{\xi})|^2) \tag{13}$$

This gives the electron hologram that can be reconstructed into a 3-D image.

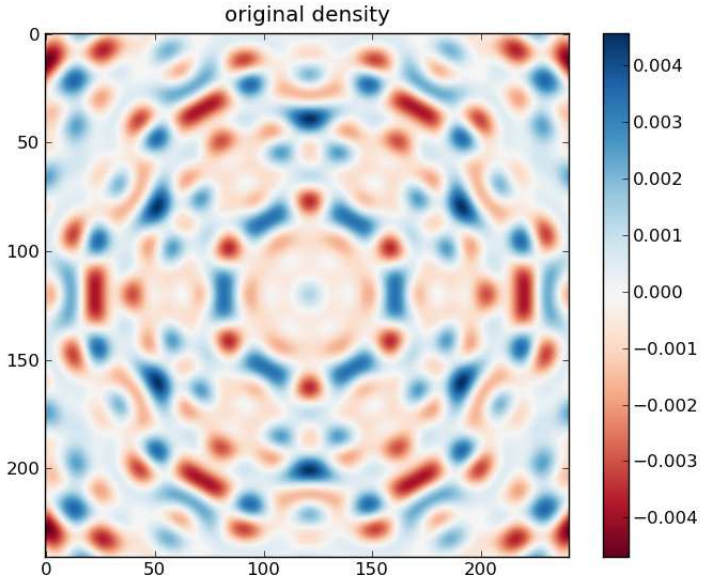

Figure 6: Theoretically generated electron hologram of benzene (C_6H_6)

Note the qualitative similarities between Fig. 6 and Fig. 5. This confirms that our simulation of electron holography is in fact providing us with accurate holograms.

The interference pattern can be decomposed in a different way into two components as is shown below:

$$I = A_0(\vec{r})e^{i\phi(\vec{r})} \tag{14}$$

where $A_0(\vec{r})$ is the amplitude and $e^{i\phi(\vec{r})}$ is the phase component. The key reason that a 3-D reconstruction can be obtained from a 2-D interference pattern is because in addition to the amplitude, the phase information is recorded.

Figure 7 shows the interference pattern split into its amplitude and phase, respectively. It is immediately obvious that the phase image has two mirroring images of the benzene molecule. This is a documented effect of seperating the phase and amplitude from an interference pattern [25]. While this creates a nice visual representation of why a 3-D reconstruction is possible, we do not use these images in our reconstruction process. Instead, we define

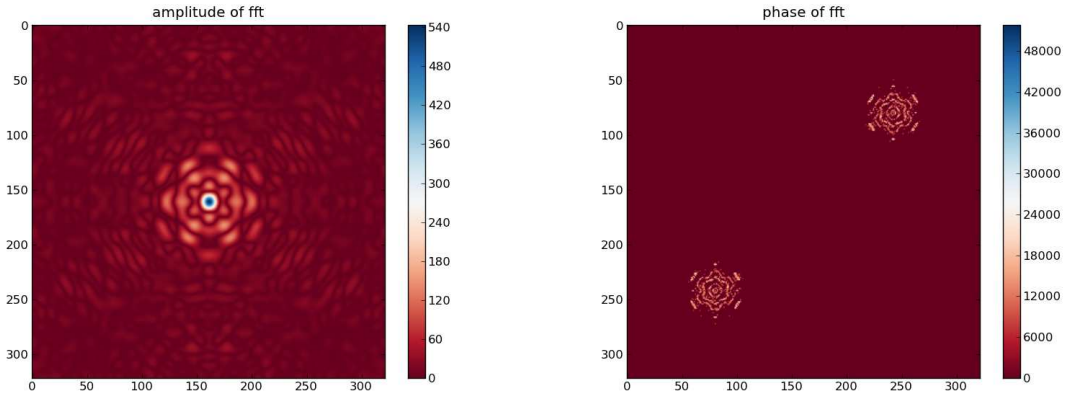

Figure 7: Electron hologram of a benzene molecule (C_6H_6) taken at the end of a 4 fs simulation split into its two seperate components: amplitude and phase, respectively.

a function, $K(\vec{r})$ in the vicinity of the target. This function creates a 3-D image of the target from the electron hologram. This image is found through the use of the Kirchoff-Helmholts transform

$$K(\vec{r}) = \int I(\xi) e^{ik\vec{\xi}\cdot\frac{\vec{r}}{\xi}} d^2\xi \tag{15}$$

where the integration extends over the the slice of density obtained from the simulation with coordinates $\vec{\xi} = (X, Y, L)$ where L is the distance from the source of the electron to the screen. In our case, the electron starts from the left most end of the box, and the screen is 22Å away, meaning $L = 22$Å. This integral is a transform from $\vec{\xi} \to \vec{r}$ where $\vec{r} = (x, y, z)$ is in the vicinity of the molecule. $I(\vec{\xi})$ is the interference pattern. Qualitatively, this integral is forming the 3-D image one 2-D slice at a time, and when it finishes, all of the slices are stacked side-by-side to form a coherent 3-D image.

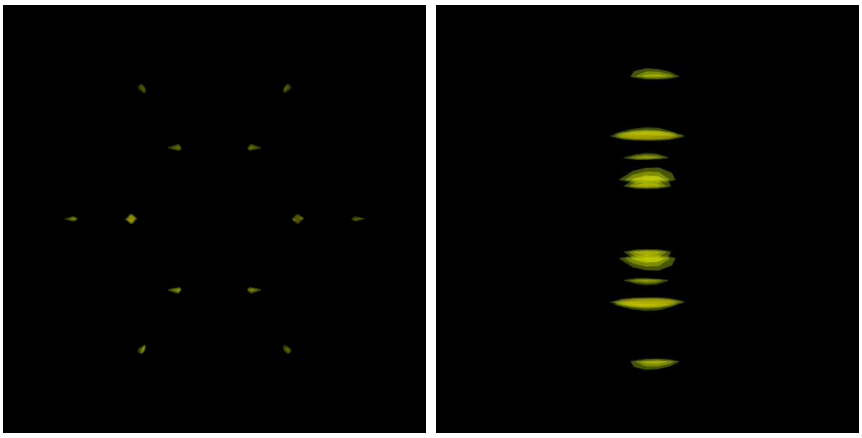

Figure 8: Two views of the 3-D reconstruction of benzene

Fig. 8 shows the results of a 3-D reconstruction of benzene. The front and side view of the molecule are shown in order to give a feel for what the 3-D image would look like. It is important to note that the raw reconstruction contains a large amount of noise that makes it difficult to see the position of the atoms. After making the proper cutoff values, Fig. 8 is what is produced. Noise reduction was all that was needed to find these images, we did not have to make any assumptions about the structure. Further work needs to be done in order to make this noise reduction case-independent. The side view of the molecule reveals a small amount of elongation. We find that the center of each shape coincides with the actual position of the molecule. When the center of each shape is taken into account, the position of the reconstructed image matches well with the position of the original benzene molecule. The problem of elongation becomes much more severe when this method is used on a bucky ball (C_{60}). Further work is needed in order to succesfully reconstruct larger molecules.

6 Conclusion

6.1 Summary

We have shown that protons are simultaneously ejected from the same molecular ion provided the laser intensity is strong enough to cause a complete molecular fragmentation. The kinetic energies of these ejected protons are very similar, and the wide distributions in the experimental spectra are caused by different spatial orientations of the molecules in the gas phase. We have also succesfully reconstructed a benzene molecule from an interference pattern by shooting an electron at the molecule. Future work in electron holography include improving our reconstruction method in order to handle larger molecules, and incorporating TDDFT into our simulations.

6.2 Acknowledgements

I thank Dr. Kalman Varga and Sergiy Bubin for all of their help and guidance throughout these two projects.

References

[1] Z. Chang *et al.*, Phys. Rev. Lett. **79**, 2967 (1997).

[2] M. Hentschel *et al.*, Nature (London) **414**, 509 (2001).

[3] R. J. Levis, G. M. Menkir, and H. Rabitz, Science **292**, 709 (2001).

[4] W. Li *et al.*, Science **322**, 1207 (2008).

[5] M. Meckel *et al.*, Science **320**, 1478 (2008).

[6] T. Ditmire *et al.*, Nature (London) **386**, 54 (1997).

[7] S. Roither *et al.*, Phys. Rev. Lett. **106**, 163001 (2011).

[8] T. Ditmire, T. Donnelly, R. W. Falcone, and M. D. Perry, Phys. Rev. Lett. **75**, 3122 (1995).

[9] A. McPherson *et al.*, Nature (London) **370**, 631 (1996).

[10] Y. L. Shao *et al.*, Phys. Rev. Lett. **77**, 3343 (1996).

[11] Z. Vager, R. Naaman, and E. P. Kanter, Science **244**, 426 (1989).

[12] J. Levin *et al.*, Phys. Rev. Lett. **81**, 3347 (1998).

[13] F. Légaré *et al.*, Phys. Rev. A **72**, 052717 (2005).

[14] A. N. Markevitch, D. A. Romanov, S. M. Smith, and R. J. Levis, Phys. Rev. Lett. **96**, 163002 (2006).

[15] C. Cornaggia, D. Normand, and J. Morellec, J. Phys. B **25**, L415 (1992).

[16] S. Palaniyappan *et al.*, Phys. Rev. A **82**, 043433 (2010).

[17] C. Cornaggia, M. Schmidt, and D. Normand, Phys. Rev. A **51**, 1431 (1995).

[18] S. Shimizu *et al.*, Chem. Phys. Lett. **317**, 609 (2000).

[19] E. Lötstedt, T. Kato, and K. Yamanouchi, Phys. Rev. A **85**, 041402 (2012).

[20] M. S. Jose Arocena, Timothy Rothwell, Micron **36**, 23 (2005).

[21] H. Kreuzer, K. Nakamura, H. F. A. Wierzbicki, and H. Schmid, Ultramicroscopy **45**, 381 (1992).

[22] M. C. Christopher Hensley, Jie Yang, Phys. Rev. Lett. **109**, 133202 (2012).

[23] D. E. Manolopoulos, J. Chem. Phys. **117**, 9552 (2002).

[24] A. N. Markevitch, D. A. Romanov, S. M. Smith, and R. J. Levis, Phys. Rev. Lett. **92**, 063001 (2004).

[25] H. Duadi *et al.*, *Holography Research and Technologies* (InTech, USA, 2011).

[26] S. Bubin, M. Atkinson, X. X. Kalman Varga, and S. Roither, Phys. Rev. A **86**, 043407 (2012).